Available online at www.sciencedirect.com
SCIENCE DIRECT®

European Journal of Mechanics B/Fluids 23 (2004) 695–708

Dynamical evolution of ripples in a wave channel

Armelle Jarno-Druaux [a,*], Jérôme Brossard [a], François Marin [b]

[a] Laboratoire de mécanique, physique et géosciences, Université du Havre, 25, rue P. Lebon, BP 540, 76058 Le Havre cedex, France
[b] Laboratoire de mécanique, physique et géosciences, Université du Havre, place R. Schuman, BP 4006, 76610 Le Havre, France

Received 17 February 2003; received in revised form 22 December 2003; accepted 9 February 2004

Available online 9 April 2004

Abstract

The dynamical evolution of ripples generated in a wave channel has been investigated using image acquisition techniques. We focus on the evolution with time of ripple geometry. A particular attention has been paid on the method used for the determination of ripple length in the transient stage. Due to the observation of numerous defects in ripple patterns during their formation, a statistical approach has been chosen. Histograms of ripple lengths distribution are processed using Hilbert transform and most probable lengths are estimated. The different stages of ripple formation are characterized by histograms with typical shapes. For some particular conditions, a temporary stable rolling-grain ripple stage can be observed, characterized by a constant most probable length for a short time interval and a constant or slowly increasing steepness. A linear dependence between the length of rolling-grain ripples and the boundary layer Reynolds number is found. In the moderate flow conditions investigated, ripple dynamics is controlled by both, the mobility number and the Reynolds number.

Keywords: Ripple dynamics; Ripple geometry; Regular waves; Visualization

1. Introduction

Due to the connection to sand transport by surface waves in near-shore regions, extensive works have been devoted to the study of ripples produced on movable beds by pure oscillatory flows. An early experimental work conducted by Bagnold [1] gives a first description of the two main classes of ripples which may be observed when destabilizing a flat sandy bed with an oscillating flow. Ones are referred to as *rolling-grain ripples*, created by the rolling back and forth of the grains, forming small triangular heaps spaced by stretches of flat bed. The others are called *vortex ripples* due to flow separation at the lee sides of the ripples responsible for vortex structures generation.

In spite of the large literature focused on ripples, this research subject is still of interest because of the partial understanding of the complex physical processes involved in ripple formation under oscillatory conditions. The present work deals with ripple morphodynamics with an original experimental methodology in order to approach ripples study in a different way. The different stages of ripple formation are investigated from the beginning of sediments motion to vortex ripples.

Of course, over the years, some interesting results have already been obtained, particularly in the domain of vortex ripples at their equilibrium stage which are the ones observed in nature. The morphological parameters widely investigated are the length and steepness of vortex ripples because they are required for the elaboration of predictive methods for sediment transport. Most of the studies refer to controlled laboratory small-scale experiments performed in various facilities: oscillating trays, oscillatory flow tunnels, wave channels; with different “sediments”: sand, plastic, glass. Many experimental results are summarized by

* Corresponding author.
E-mail address: armelle.jarno-druaux@univ-lehavre.fr (A. Jarno-Druaux).

0997-7546/$ – see front matter
doi:10.1016/j.euromechflu.2004.02.002

Sleath [2]. The dependence of bed form morphology on the mobility number which is the square of the Froude number is clearly demonstrated in the different installations tested. Nevertheless, a substantial scatter between the different sets of data is noted. Part of this discrepancy can be explained by the influence of the flow Reynolds number. Even for moderate flow conditions, the wavelength scaled by a, the fluid-orbit amplitude at the edge of the boundary layer is not simply a constant value but is a function of both mobility and Reynolds numbers (Faraci et al. [3]). Other factors can explain partly the observed differences. First, in most of the experimental studies reported, no specific instrumentation is used to determine the dimensions of the ripples and their estimation is mostly a local measure in spite of irregularities in ripple patterns. Furthermore, it is worth pointing out that the final state of vortex ripple patterns remains dynamical and that locally, the wavelength can be greatly influenced by the development of long-time instabilities (Voropayev et al. [4]). At last, except in some recent studies, the time necessary for the ripples to reach their mature state is often estimated subjectively.

Rolling grain ripples are of minor direct practical interest because they have never been observed in field. However, it is an interesting case of forced dynamical system. If we refer to recent studies conducted under very controlled experiments in one-dimensional annular geometries, rolling-grain ripples always destabilize (Scherer [5], Stegner et al. [6]). Furthermore, there is a global comprehension of the process leading to ripple formation under oscillatory flow conditions. The interested reader can look at the papers of Sleath [7] or Kaneko et al. [8]. It is found that ripple growth is due to steady streaming induced by Reynolds stresses in the Stokes layer. Two different theoretical approaches are proposed to study rolling-grain-ripples. In the first one, rolling-grain-ripples are considered as an hydrodynamic instability. Then, the geometrical configuration of initial ripples can be determined by a weakly nonlinear stability analysis (Blondeaux [9], Vittori and Blondeaux [10]). The extension of this work to investigate wave-current ripples was recently proposed (Blondeaux et al. [11]). The introduced dimensionless independant parameters are the Froude number F_D and two Reynolds numbers R_D and R_δ based respectively on the mean sediment diameter and Stokes layer thickness. The second approach is a granular approach (Andersen [12]). In a particle model elaborated for the formation of rolling-grain ripples, an equation of motion is written for each ripple considered as a particle interacting with its neighbours. Even though a lot of theoretical works are devoted to ripple formation, the experimental investigations reporting rolling-grain ripple characteristics (Manohar [13], Sleath [7], Blondeaux et al. [14], Blondeaux et al. [11], Rousseaux et al. [15]) are still very few to validate theoretical works and the results are dispersed. This may be partly due to the difficulty to study experimentally this transient state. Furthermore, according to Rousseaux et al., the selection of the initial length of one-dimensional ripples can be studied only for weak forcing cases with a careful initial preparation of the bed.

The application of more sophisticated experimental techniques and processing data turns out very useful to extract more accurately the geometrical characteristics of ripples and to provide information on the dynamical evolution of the rippled bed profiles. An acoustic method is utilized in field by Hanes [16] to measure ripple dimensions. Representations of lengths distributions in the form of histograms are then adopted because the ripples are not perfectly uniform and periodic and can exhibit simultaneously two scales of bed form lengths. Another experimental methodology based on the image processing of video recordings from a "slice" of cross-sectional rippled sand beds lighted by a laser sheet is used by Faraci et al. [3] in a wave tank. In this work, it is clearly pointed out that the evolution with time of the height and length of individual ripples may significantly differ.

Consequently, the evaluation of mean morphological parameters on short fields does not seem to be sufficient to understand the complex mechanisms involved in ripples formation. Additional information are needed to investigate accurately ripple patterns exhibiting irregularities and local defects. In this paper, the morphodynamics of ripples formed by a gravity wave in a channel is addressed. In this specific bidimensional geometry, pattern defects are numerous and participate in ripple growth. This has motivated the development of an analysis technique based on the statistical analysis of extended bidimensional patterns. After a presentation of the installation used, the techniques employed are described (Section 2). Both top views on large fields and side views on a line are performed giving complementary information. The image processing developed for the two views is explained. Section 3 is devoted to the description of qualitative observations and particularly to the analysis of the shape of the histograms of lengths distributions associated with different typical stages of ripple formation. Section 4 is dedicated to the results and interpretations. Finally, the main conclusions are given in Section 5.

2. Experimental set-up and investigating techniques

2.1. Experimental set-up

The experiments were conducted in a wave flume at Le Havre University. The test section is 10 m long, 0.49 m wide and 0.5 m high. A general view of the channel is shown on Fig. 1.

The desired oscillatory motion is created by a piston-type wavemaker situated at one end of the channel. At the other end, an inclined beach made of porous filters is used to absorbe the energy of waves. A particular attention has been drawn to control the quality of the monochromatic waves generated. Then, an original technique developed by Brossard et al. [17] based on the

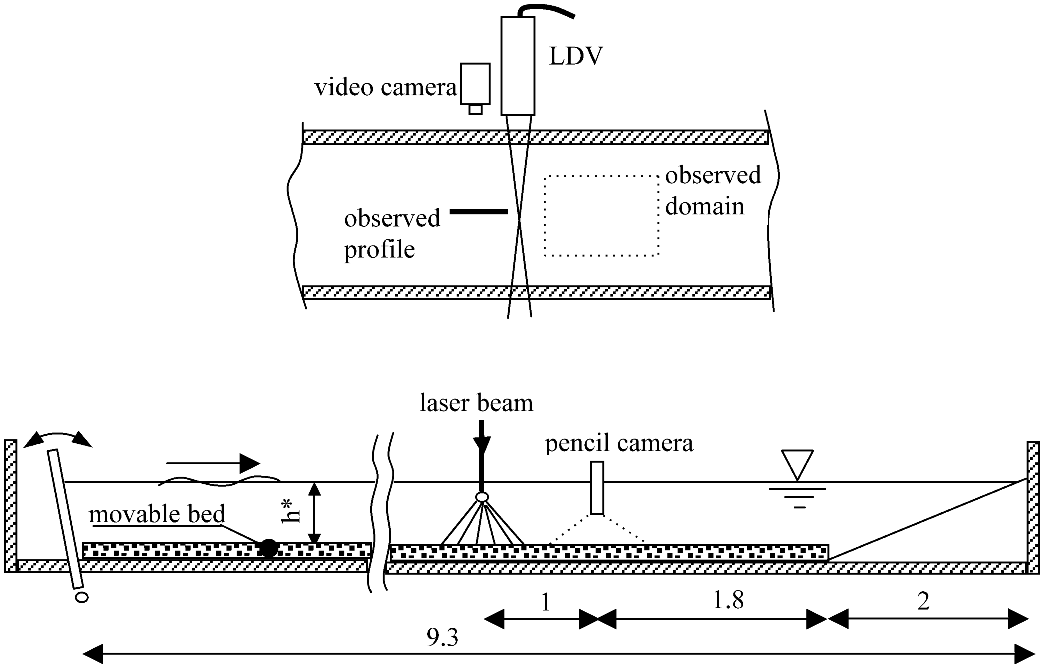

Fig. 1. General view of the channel and instrumentation.

analysis of the signal issued from two moving resistive level probes is used. We access to the parameters of the free surface (period T, wave height H) and to the wave reflection coefficient with a great accuracy.

Some preliminar tests conducted with ramps used to bound a limited test bed (3 m-long) show that the quality of the free surface is affected by the experimental set-up. Then, it was chosen to fully cover the 10-m-long test section of the flume by sediments on a 2.5 cm thickness. Finally, the measured reflection coefficient during the tests is less than 6%.

The fluid motion in the test section is controlled by the simultaneous measurement of the horizontal and vertical components of velocity using a two-component Laser Doppler Velocimeter at one-ripple wavelength above the bed. The maximum horizontal velocity measured at this height gives a convenient estimation of the maximum velocity outside the wall boundary layer. The measured values are very near (less than 5%) to the ones estimated by the 2nd order Stokes model.

2.2. The top view

A pencil camera (Panasonic, GP-KS162HDE) equipped with a lens of short focal length (3 mm) is immersed under the free surface. This instrumentation provides a large top view visualisation of the ripple pattern that is acquired continuously. In practice, the camera is situated sufficiently far from the movable bed to be sure of its minor influence on bed ripple formation. The orientation of the camera is chosen in order to cross the maximum number of ripples. Then, the horizontal x-*axis* of the collected images is parallel to the propagating wave direction and the vertical y-*axis* refers to the cross-section direction. On the images presented below, the waves propagate from left to right. The dimension of the observed domain is 280 mm long and 220 mm wide. The spatial resolution for this view is equal to 0.49 mm/pixel. A small distortion of the edges of the images due to the short focal length is observed but no correction was required because the image is partially cropped before being processed.

The light intensity distribution of each line composing the images collected from this view is sampled in 256 values displayed in grey levels. It can be noted that the measured intensity is not proportional to the elevation of the ripples but is a function of their slopes.

An image processing has been developed to provide accurate local information in the ripple patterns and collapse these information plotting the distribution of ripple wavelengths. The technique used is the complex demodulation. It has been accomplished through the use of Hilbert Transform.

The first step of the signal processing developed with MATLAB v 5.0 software consists in reducing the number of data to 512 points/line, by cropping the image, to perform a one dimensional spatial Fourier transform on each line of the image thanks to a FFT algorithm. The negative spatial frequencies obtained in the spectral domain are redundant with the positive ones and consequently convey no more information. In a second step, these values are then set to zero and a band-pass filter adapted

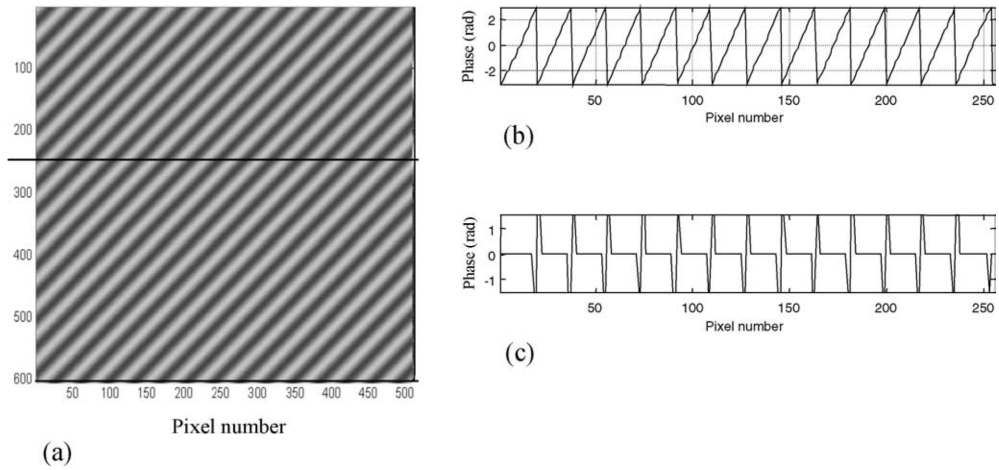

Fig. 2. Calibration of the image processing used for top views. (a) Test image; (b) phase signal $\phi(x)$ on a chosen horizontal line; (c) spatial derivative of the phase $\partial\phi/\partial x$ on the same line.

to each image is applied. The latter consists in eliminating both, the large scale inhomogeneity in light illumination (due to the relative large size of the domain) and some small-scale noise (due to particle suspensions, for example). Afterwards, the complex demodulation is accomplished by processing the inverse Fourier transform of the truncated signals. Hence, the real signal $I(x, y)$ (the image) is replaced by its complex equivalent expression $\underline{I}(x, y)$ as follows:

$$\underline{I}(x, y) = \left|\underline{I}(x, y)\right| \exp \mathrm{i}\phi(x, y),$$

where $|\underline{I}(x, y)|$ and $\phi(x, y)$ represent respectively the amplitude and phase of the complex signal.

The main information is contained in the phase signal. The process consists in locating the sudden phase jumps from $+\pi$ to $-\pi$ associated with the detection of ripples. Forming the spatial derivative of the phase along the x-axis provides an easy way to estimate accurately the local wavelength. A threshold is fixed to locate the ripple positions and thus, the distance between neighbouring ripples can be easily calculated. Finally, the distribution of wavelengths in the image is plotted in the form of an histogram, after a compilation of the data on all the lines.

The technique is illustrated on an example in Fig. 2. We show a test image built on a unique wavelength (a) used to calibrate the technique, the phase signal on a line (b) and the associated spatial derivative (c). The calibration of the technique with "a perfect pattern" gives a Dirac peak at the correct wavelength. This result reveals that the Hilbert transform is insensitive to the finite length of the image. On the other hand, the direct analysis of the spectrum issued from the same image is characterized by an enlarged peak.

Furthermore, a correction is necessary to validate the obtained wavelengths. It is clear that for a fixed length, the maximum number this length can be measured is conditioned by the size of the observation field. This number is not a constant but varies with the inverse of the ripple length. Therefore, it is required to weight, for each length, the number of ripples detected by the maximum number of ripples that could be detected in the investigated field for the considered length. Further on, a statistical representation is plotted by normalizing the lengths distribution. If the length distribution is considered as a quasi continuous function, the histograms can be analyzed in terms of probability distribution function of wavelengths in the observed field. From the histogram, we extract a mean wavelength $\bar{L}$ and a most probable wavelength L_p. Other data can be determined to give additional information on the lengths distribution (root mean square of the distribution, half-width, higher orders momentum for example) but they are not reported in this paper.

As was mentioned above, the resolution of the technique is fixed to 0.49 mm/pixel. But, the accuracy of the technique is difficult to estimate. In particular, in this study, the accuracy cannot be estimated by the standard deviation of the lengths distribution since ripple patterns considered herein are not perfectly regular and consequently introduce an enlargement of the histograms.

2.3. The side-view

A thin vertical light sheet is generated in the middle section of the channel by a focused laser beam pointing a cylindrical lens. The sediments are illuminated and the intersection of the laser plane with the bed produces a line ~ 200 mm long which follows the morphology of the movable bed. The latter line viewed from the side of the flume is video recorded with a Panasonic video camera. A preliminary calibration of the images is performed. This operation is achieved by focusing on one known object positioned in the laser plane section where ripples are observed, and recording the obtained image to calculate the resolution. This latter one is estimated to 0.17 mm/pixel, that is to say of the order of the grain diameter.

Similarly to the top view, the acquired images of the bedform are processed at the end of each test. Although an automatic detection of ripple morphology could seem at once to be the better solution to process the large amount of collected images, a manual analysis was preferred. This choice is due to suspended particles which may be illuminated identically to particles at the bed and then should lead to an erroneous ripple detection. Therefore, a manual determination of the wavelengths and heights of the ripples on selected frames chosen both at the same period phase and at chosen instants to follow the time evolution is performed. An averaged value of the side view wavelength L_s and height h over ~ 10 ripples is calculated. The observed ripples are irregular. Then it is chosen to estimate the mean steepness h/L_s over the ten ripples observed by averaging the steepnesses of the individual ripples observed.

2.4. *Test conditions*

The dimensions of the channel make difficult the generation of large amplitude waves and consequently, heavy particles are hard to move. Then, the experiments were conducted with light plastic particles of relative density d equal to 1.35 and a mean grain diameter D of 0.17 mm.

The static angle of internal friction for the dry sediment has been determined with a shear box. A 32.5° is found for the plastic sediment. The angle of repose is correctly approximated by the same value if dry sediment is involved. For the case of water saturated sediments, the angle of repose is affected by water's buoyancy forces and water pressure in the pores and then, the expected value of this latter angle may be smaller. Furthermore, in this case, the relationship between the two above angles may be less evident.

Table 1 shows the experimental conditions for the tests. Sixteen experiments were carried out for two different water depth h^*. Included in Table 1 are the values of the dimensionless parameters used to study the global dynamics of the ripples. The mobility number $\psi = (a\omega)^2/(s-1)gD$ varies in the range 2 to 13. The skin friction Shields parameter $\theta = 0.5 f_w \psi$ is defined with Jonsson [18] formulae for the skin friction factor f_w and the flow Reynolds number R is given by $a^2\omega/\nu$. In these formulae, s stands for the specific gravity, ω is the frequency and a denotes the fluid-orbital amplitude at the edge of the boundary layer.

The water temperature was measured regularly and used to calculate accurately the fluid kinematic viscosity ν.

Each test begins after an initial preparation of the non-cohesive bed consisting in flattering it. This important preliminary task is performed by both, rolling a grid over the bed to "break" the ripples of the preceding test and dragging several times a levelled screen. A two-hour measurement period is investigated for each test. Reminding the range of wave periods considered herein, we have chosen to study the first 6000 excitation periods. It is expected to exceed, for each test condition, the number of cycles required to reach an equilibrium ripple geometry.

The video recording procedure defers for the two views. For the top view, the images are collected continuously for a 50 min duration. Then, the recording is stopped and an additional ten minutes record is performed at the completion of the test one hour later.

Table 1
Experimental conditions of the tests and dimensionless parameters

Test n°	T (s)	H (m)	h^* (m)	a (m)	Ψ	θ	R
1	0.8	0.031	0.27	0.0054	3.2	0.205	237
2	0.8	0.045	0.27	0.0080	6.8	0.305	498
3	1.1	0.023	0.27	0.0087	4.3	0.207	441
4	1.1	0.036	0.27	0.0134	10.2	0.313	1063
5	1.1	0.044	0.27	0.0161	14.7	0.372	1565
6	1.4	0.023	0.27	0.0123	5.3	0.196	738
7	1.4	0.032	0.27	0.0169	10.0	0.272	1360
8	1.4	0.026	0.27	0.0136	6.5	0.216	900
9	0.8	0.049	0.35	0.0050	2.7	0.187	214
10	0.75	0.068	0.35	0.0062	4.3	0.231	354
11	1.1	0.035	0.35	0.0098	5.5	0.220	622
12	1.1	0.046	0.35	0.0125	8.9	0.280	1015
13	1.1	0.054	0.35	0.0151	12.9	0.333	1505
14	1.33	0.028	0.35	0.0110	4.7	0.182	665
15	1.33	0.035	0.35	0.0142	7.8	0.237	1087
16	1.33	0.045	0.35	0.0180	12.7	0.303	1764

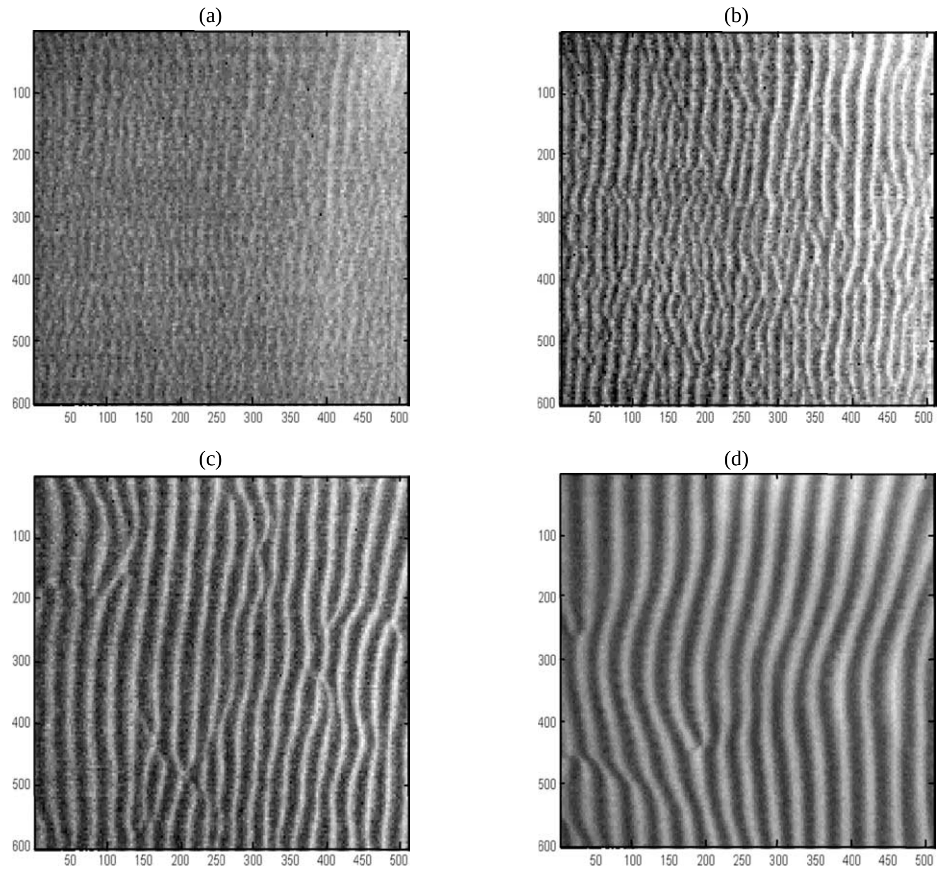

Fig. 3. Examples of top views at different stages of ripple development with time (Test 2). (a) First excitation cycles; (b) rolling-grain ripple state; (c) intermediate state; (d) vortex ripples.

For the side view, the sample scheme is divided in three parts: (1) a 10 min continuous acquisition from rest; (2) another 10 min record, 50 min later and (3) a last 10 min record at the end of the run. The two views are synchronized by using leds controlled by the motion of the wave maker that can be observed in the field of the cameras.

3. Qualitative observations

Different observations of ripples formation have previously been described by Lofquist [19], Traykovski et al. [20] and O'Donoghue et al. [21] in both field and laboratory two-dimensional experiments. Furthermore, the process exhibits some similarities with the one described in a one-dimensional annular geometry installation (Stegner et al. [6]). In present study, the processing technique is used to get more information on vortex ripple formation. The scenario of vortex ripples formation is broadly similar from a test to the other. It will be illustrated by test 2.

The tests begin from rest with a flat bed. The paddle oscillations are then initiated with an amplitude displacement controlled to produce a sufficient motion to generate ripples. A few seconds later, individual superficial grains begin to move back and forth to form a complicated network of short fragments of three-dimensional ripples. Fig. 3(a) provides an example of top view observed during the first time-instants of ripples formation, revealing the non-organized nature of the ripples pattern. The image contrast is not very good because of the low height of ripples. The associated distribution of ripple lengths (Fig. 4(a)) is characterized by an enlarged peak of weak amplitude lenghtened by a long train exhibiting a large variety of long length scales. In these conditions, the comparison of $\bar{L}$ and L_p gives a mean value larger than the most probable one ($L_p < \bar{L}$). Furthermore, in a one-dimensional geometry, it was pointed out by Rousseaux et al. [15] that the observation of the initial wavelength for rolling-grain-ripples is only possible for very weak amplitude motions. In present two-dimensional geometry, the process leading to the first ripples formation is not a selective process for the wavelength even for the lower values of the mobility parameter tested. Consequently, the estimation of the initial wavelength for the rolling-grain-ripples is never possible.

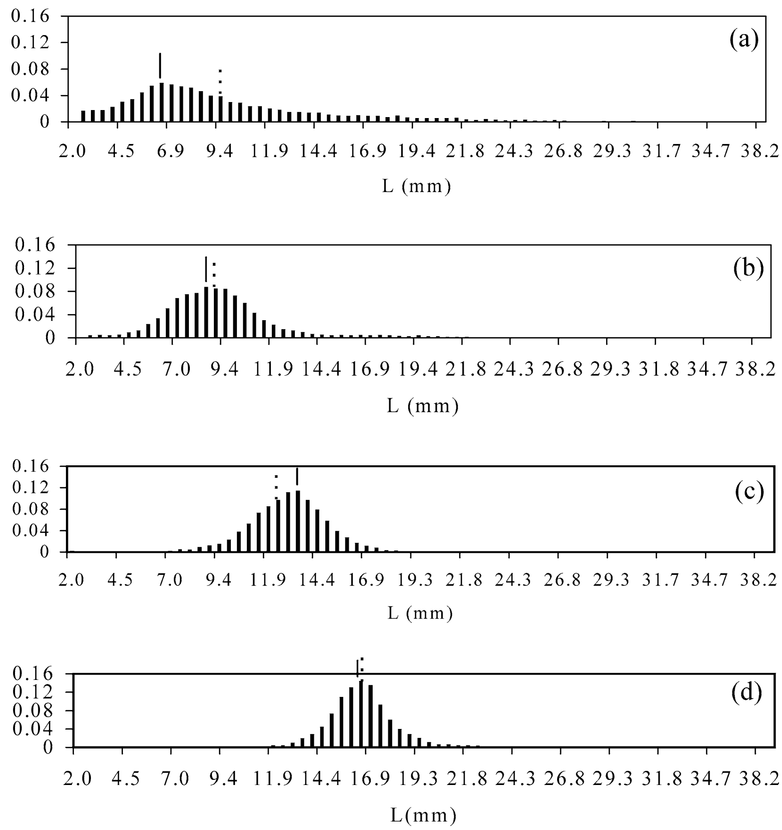

Fig. 4. Histograms of lengths distributions associated to the top views from Fig. 3. Short black lines and dotted lines denote respectively the most probable length and the mean length of the distributions.

A few seconds later, many annihilations of defects are observed and reconnections of 3D ripples lead to the formation of a two-dimensional organized pattern with ripples align with a mean direction perpendicular to the generated wave. The shape of the histogram (Fig. 4(b)) differs significantly from the former. It is more symetric, not very sharp because of many defects, and characterized by a mean length slightly higher or of the same order than the most probable one ($L_p \leqslant \bar{L}$). The observed pattern corresponds to a pattern that we identify as an organized *rolling-grain ripples* (Fig. 3(b)) state. However, this regime is only observed when the amplitude motion is weak enough. If we wait enough longer, these ripples destabilize and evolve spontaneously in height, shape and length to emerge finally in the form of *vortex ripples* (Fig. 3(d)). It can be seen from the histogram (Fig. 4(d)) that lengths have been shifted towards longer values. The distribution still remains large, demonstrating that a final state without defects and irregularities is never reached. However, it can be noticed that the distribution of lengths is typically characterized by a mean value nearly equal to its most probable one ($L_p \approx \bar{L}$). An intermediate state is represented on Fig. 3(c). A deformation of the associated histogram (Fig. 4(c)) is noted, due to an increase of the number of lower lengths detected in the image ($L_p > \bar{L}$). The histogram shape shows that a reconnecting process of the ripples takes place. Here, the ripple coarsening process is different from the one described in one-dimensional geometries because of the important role played by 3D defects in the pattern dynamics.

4. Results

4.1. Ripple growth evolution with time

Before examining further the ripple length evolution with time, a preliminary study is aimed at comparing the three different estimation methods for the wavelength in order to select, in our sense, the most representative one. The three processed wavelengths are the side wavelength L_s, the mean wavelength $\bar{L}$ and the most probable one L_p.

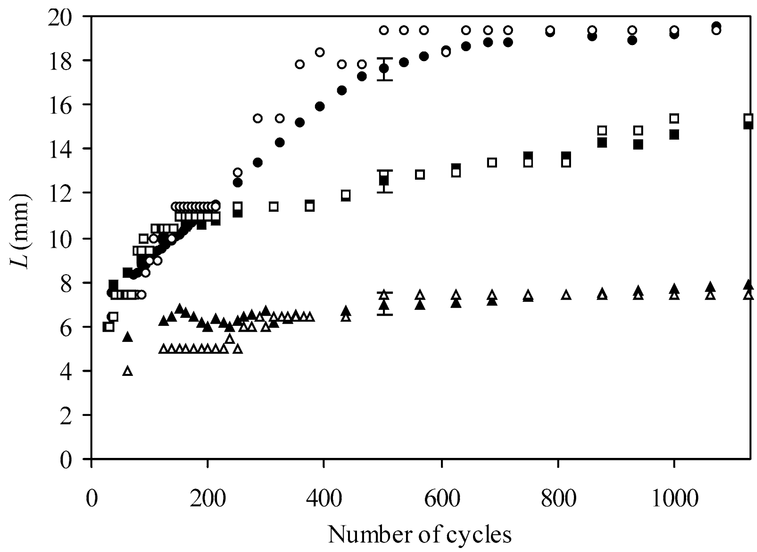

Fig. 5. Wavelength ripple versus the number of excitation cycles. Black point: mean wavelength $\bar{L}$; white point: most probable wavelength L_p, △, ▲: Test 9; ○, ●: Test 6; □, ■: Test 2.

Since tested ripple patterns are never completely regular, the estimation of a mean wavelength from the side view is not very accurate because of the short length of the observed line. Therefore, a statistical determination on a wide two-dimensional field may provide a better estimation. Thus, the time evolutions of both the mean wavelength $\bar{L}$ and the most probable wavelength L_p are plotted on Fig. 5 for three different mobility numbers. The thousands first excitation cycles are represented with a representation of the typical accuracy fixed to the resolution on this view.

The results show a rather good agreement for long excitation durations but exhibit substancial differences during the initial stage of ripple formation. The observed convergence between the two estimations suggests that, in the processed field, an organized vortex ripple pattern develops whose mean length is no more noticeably affected by defects. Furthermore, it is demonstrated that the observed field is large enough to verify the conservation of the mean length for long times. Of course, there are still persistent defects, but their density becomes both low and nearly constant when the ripple pattern dynamics slows down. The quasi-equilibrium length reached is noted L_{eq}.

At the early stage, the evolution curves for the two lengths can significantly differ. It is seen that the mean length evolves rather regularly while the most probable one exhibits a progression by steps. It demonstrates the interesting result that a more present wavelength L_p can remain constant for a short time interval in an evolving pattern characterized by a mean length which varies continuously. As illustrated in the previous section, a detailed examination of Fig. 5 indicates that, at the beginning, the mean ripple length tends to be greater than the most probable one due to the discontinuous distribution of 3D ripples of low wavelengths on the bed. Then, when processing the Hilbert transform on the lines of these images, long wavelengths can be measured when the short fragments of 3D ripples are not crossed. Later, this trend reverses due to the contribution of numerous low length defects in the generated 2D ripples. The ripple dislocations contribute to the increase of the wavelength ripples pattern. The number of cycles for the inversion to occur seems to be a function of the mobility number.

Hence, due to the sensitivity of $\bar{L}$ to defects involved in ripple patterns during the transient stage, the estimation of the length by the most probable one will be chosen to study further ripple dynamics.

For studying the global evolution of the ripple wavelength with time, a representation of L_p normalized by its equilibrium value L_{eq} is plotted in Fig. 6 as a function of a non-dimensional time t/τ for all the tests. As proposed by Voropayev et al. [4], the typical time τ is given by $\tau = c/\omega\psi^{1/2}$ where c is a constant used to fit the data by the following exponential law: $L_P/L_{\mathrm{eq}} = 1 - \exp -t/\tau$. Identically to Voropayev, the best fit for our data is obtained for $c = 2500$. In the present study, only one type of sediment is considered. Then, the reduced gravity force remains constant in all the tests and the ψ variation is only due to the fluid velocity amplitude U_0 variation. Therefore, an increase of U_0 involves an increase of ψ and consequently, it is responsible for a decrease in the duration of the formation period. The general trend of ripple growth evolution with time may be roughly captured by an exponential law but the agreement is not as good as in Voropayev study performed on standing waves. Some features cannot be taken into account by the latter law. First, the scatter of the data for short times is due to the existence, in certain cases, of time intervals characterized by a constancy of the most probable wavelength in the pattern. This time domain is studied further in next paragraph. Second, for a fixed dimensionless time, the ripple most present length seems to be affected by the Reynolds number: ripple length increases when increasing the Reynolds number. It was previously pointed

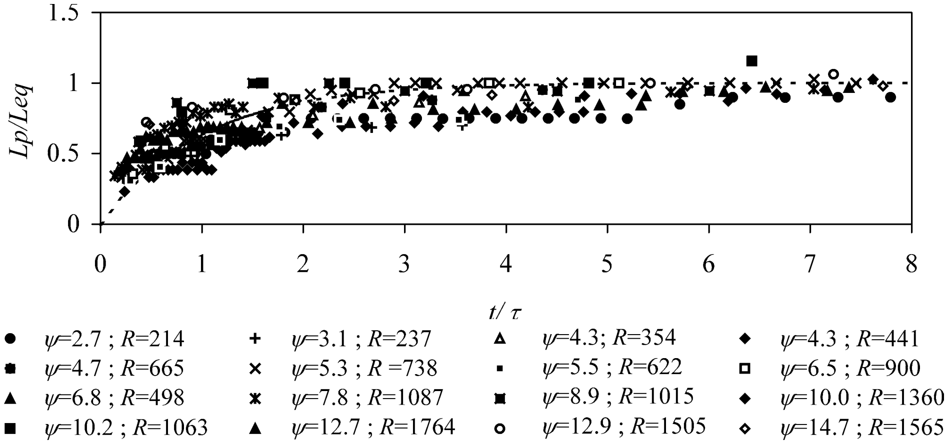

Fig. 6. Normalized representation of ripple length L_p/L_{eq} plotted versus a dimensionless time t/τ for the 16 tests. Dotted line shows the exponential law.

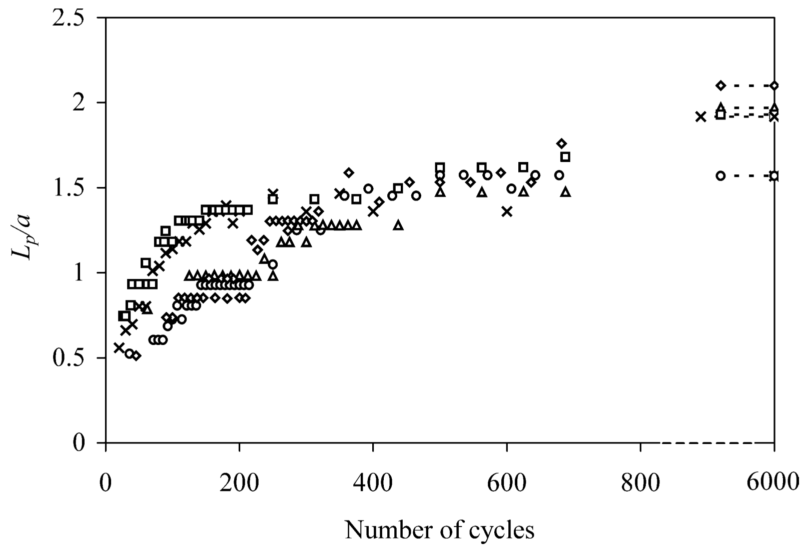

Fig. 7. Development of ripple length L_p/a with time for the first 700 excitation cycles. □: Test 2; ◇: Test 3; ○: Test 6; △: Test 9; x: Test 15. The final measured lengths are represented by dotted lines.

out that the equilibrium state of vortex ripples under moderate flow conditions (Faraci et al. [3]) was influenced by both the Froude and Reynolds numbers. Here, it is demonstrated that the dependence on these two parameters is also marked in the dynamical stage of ripple formation. The number of cycles necessary to reach a stable dynamical equilibrium of the movable bed is noted n_{eq}. It is estimated by 3τ, leading to 95% of the equilibrium length reached. In the range 3 to 15 for the mobility numbers considered herein, it gives n_{eq} in the range ~ 700 cycles for the lower ψ values and ~ 300 cycles for the higher ones. A comparison between present results and previous data (Lofquist [18], Faraci et al. [3], Voropayev et al. [4], O'Donoghue et al. [20], Stegner et al. [6]) shows that the time scale estimation for vortex ripple formation can vary significantly from a work to the other. Reported recent results lead to either comparable estimations of the ripple formation durations [4] or larger ones [6,20]. Thus, in an annular channel (1D geometry), for weak oscillation ($\psi \sim 3$), 10–14 days may be needed to reach a final state [6]! In the light of this result, a further examination of the lowest mobility number test performed (test 9) reveals that the equilibrium ripple shape ($h/L_s = 0.13$) is not certainly reached after 2 hours. In addition, it is also worth pointing out that the bed porosity is a sediment parameter which is ignored in the interpretation of our results in spite of its possible influence on ripple dynamics. Furthermore, the initial compaction of the bed may have a significant influence during the initial stage of the bottom time development. Consequently, the time establishment of equilibrium ripple patterns is also probably influenced by this parameter. Finally, it is suggested that estimation of vortex ripple formation times are to be predicted with care.

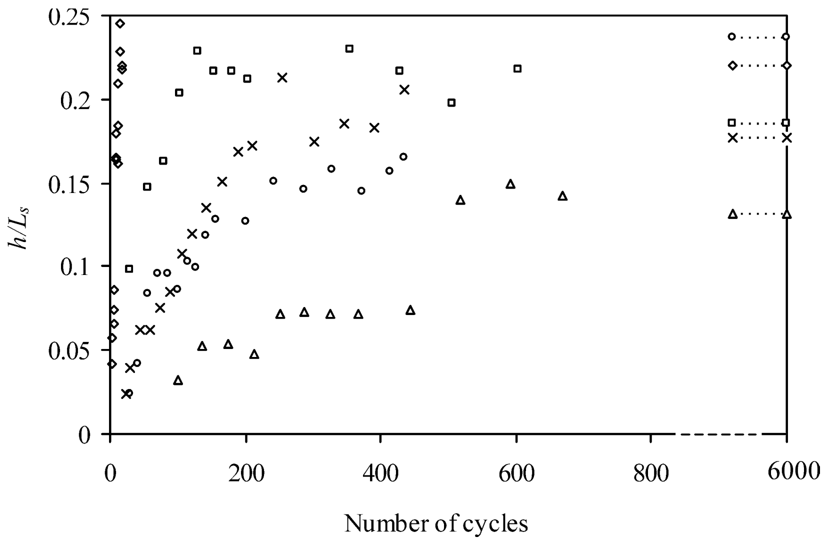

Fig. 8. Development of ripple steepness h/L_s with time for the first 600 excitation cycles. Symbols are the same as in Fig. 7.

4.2. Rolling-grain ripples

In order to study the initial stage of ripple formation, the ripple length L_p/a is plotted on Fig. 7 for five mobility numbers, as a function of a restricted number of excitation cycles, fixed to 700 cycles. The short dotted lines at the border of the plot denote the L_{eq} measured values after ~ 6000 cycles. As was suggested above, the most probable wavelength encountered in the observation field is insensitive to minor changes in the pattern. Therefore, in certain test conditions, a remarkable saturation of the length at a given value can be detected. Provided that the associated ripple steepness h/L_s remains small and that no noticeable separation of the flow is observed, the constancy of the length can be interpreted as the detection of a stable rolling-grain-ripple stage for a short time interval. The longer steady states can last $\sim$ 100–200 cycles for the lower mobility numbers. This state is followed by a rapid increase of the most present length of the pattern, suggesting that the ripple formation process becomes different. For the larger mobility number plotted ($\psi = 7.8$), the very initial stage of ripple formation is characterized by a steep increase of L_p/a without detection of a temporary stable rolling-grain ripple stage. In this case, the rolling grain ripples develop into vortex ripples without reaching an obvious transient equilibrium state. Then, the absence of temporary stable rolling-grain ripple state is not only related to the irregularity of the waves (Faraci et al. [13]) but also clearly depends on the mobility number.

In Fig. 8, the ripple steepness h/L_s is shown as function of the first 600 excitation cycles for the same five mobility numbers shown in Fig. 7. The accuracy on h/L_s is not very good because of the addition of measurement errors on both the height and the wavelength of ripples and because of the few number of ripples observed on this side view. Anyway, for the two lowest mobility numbers plotted, a sudden change in the ripple growth rate is noted when ripple steepness reaches approximately $h/L_s = 0.1$. This value coincides with the empirical criterion proposed by Sleath [7] to classify rolling grain ripples and vortex ripples. However, when $h/L_s < 0.1$, the ripple steepness does not maintain at a constant value during a significant number of cycles, except for the $\psi = 2.7$ case. Furthermore, it can also be verified that the constant stage for the ripple length observed in Fig. 7 is associated with low steepness ripples ($h/L_s < 0.1$). Finally, we characterize a temporary stable rolling-grain ripple state by both, a steepness nearly equal to 0.1, a constant most probable wavelength and a constant or weakly increasing mean ripple height. The absence of saturation of the height of rolling-grain ripples except for the lower mobility number shows that the spacing between ripples seems to be more stable than ripple height. A constant spacing between ridges can maintain whilst sediments pile up and raise up, increasing both the length and height of the triangular heaps of the ripples. This phenomenon lasts till a critical height is reached. Then, separation of the flow becomes dominant and both, the height and length of the ripple increase.

A rough estimation of n_c defined as the number of excitation cycles necessary to reach the critical steepness value ($h/L_s = 0.1$) has been performed. Before comparing the n_c values for the different tests, it is worth bearing in mind that the same experimental procedure has been conducted before each test to re-flatten the bed. Then, the initial state of the bed remains broadly identical from one test to the other. A comparison with other data would be more doubtful. A representation of n_c is plotted on Fig. 9 as a function of the mobility number. The filled circles denote the cases where a “stable” rolling grain ripples stage has been clearly observed (characterized by a stage with constant wavelength) and the empty circles refer to the

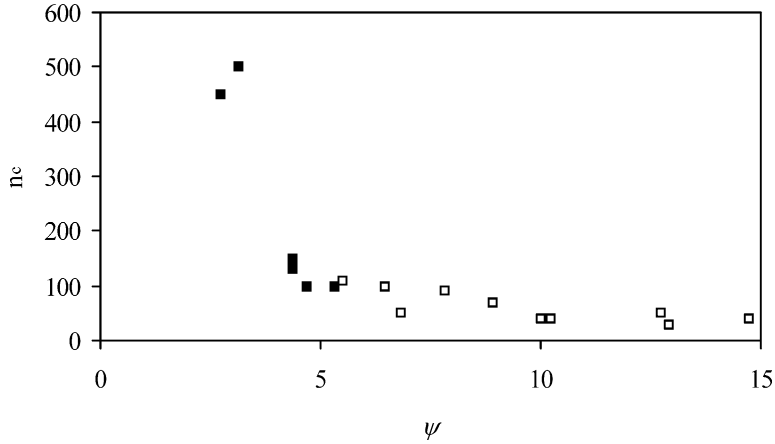

Fig. 9. Number of excitation cycles necessary to reach the critical steepness value 0.1 as a function of mobility number. ■ Observation of a rgr stable stage for a short period; □ no detection of temporary stable rolling-grain-ripple state.

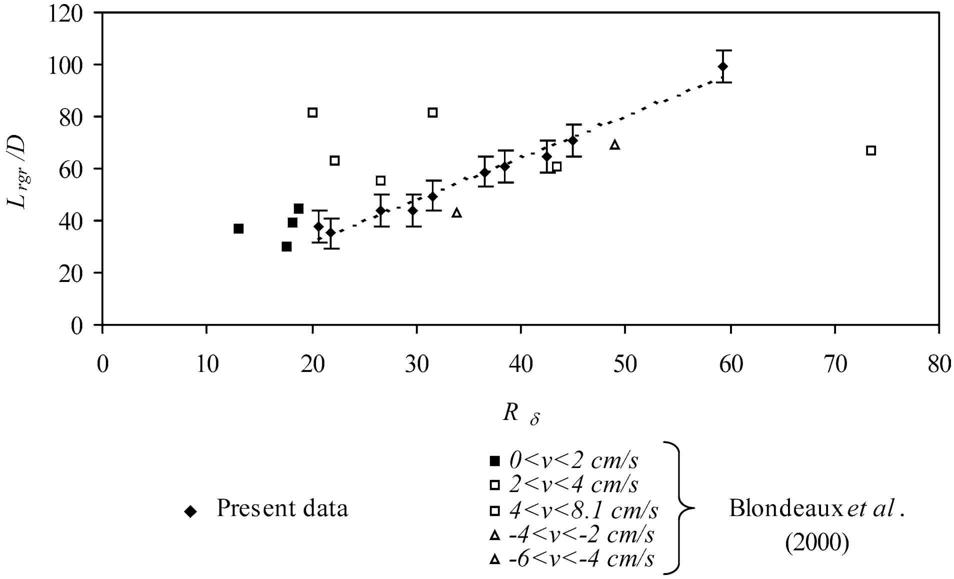

Fig. 10. Measured rgr wavelength L_{rgr} normalized by mean grain diameter D as a function of R_δ. On the same plot, data from [11] obtained for different ranges of ripple migration speed v. The dotted line shows the linear dependence between present data and R_δ.

cases where no temporary stable rolling-grain ripple state has been found. It is pointed out that the n_c value quickly decreases when increasing the mobility number. When $\psi > 8$, n_c becomes lower than 100 excitation cycles and when $\psi > 5.5$, no stable stage is observed. Therefore, the domain of rolling grain ripple existence is very restricted.

The geometric characteristics (L_{rgr}, h) of rolling-grain ripples are given in Table 2 together with the three dimensionless parameters generally used to study the first stage of ripples: $R_\delta = U_0\delta/\nu = (2R)^{0.5}$, $R_D = U_0 D/\nu$ and $F_D = \psi^{0.5}$. It is worth noticing that this part of work concerns only 9 tests. Here, only the tests exhibiting a "stable" rolling-grain stage are considered. The rolling-grain ripple wavelength L_{rgr} is estimated from the top view by its most probable value during the stable rolling-grain-ripple stage. Ripple heights are estimated for $h/L_s = 0.1$. A representation of L_{rgr}/D as a function of the boundary layer Reynolds number is displayed on Fig. 10. In the domain of parameters tested, it is clearly shown that the wavelength of rolling-grain ripples depends linearly on the boundary layer Reynolds number. Furthermore, the measured lengths are compared with Blondeaux et al. [11] data which were also performed in a wave channel with plastic particles having a median diameter D equal to 0.35 mm and 0.54 mm. In this work, the wave conditions are chosen in order to generate a nonnegligible steady drift on the bottom. The migration speed v of the ripples is measured together with the ripple length and height. The results of Fig. 10 indicate that present data with no noticeable steady current separate data with positive drift from those with negative

Table 2
Geometric dimensions of rolling-grain ripples (rgr) and dimensionless parameters

Test n°	L_{rgr} (mm)	h_{rgr} (mm)	R_δ	R_D	F_D
1	5.96	0.38	21.8	7.5	1.8
2	8.42	0.58	31.6	10.6	2.6
3	7.44	0.55	29.7	8.6	2.1
4	/	/	46.1	13.5	3.2
5	/	/	55.9	16.5	3.8
6	10.3	0.79	38.4	10.2	2.3
7	/	/	52.2	13.7	3.2
8	11	1	42.4	11.3	2.5
9	6.44	0.48	20.7	7.2	1.6
10	/	/	26.3	9.2	2.1
11	/	/	35.3	10.7	2.3
12	12	1.15	45.1	13.8	3.0
13	/	/	54.9	17.0	3.6
14	10	0.97	36.5	10.3	2.2
15	/	/	46.6	13.0	2.8
16	16.87	1.67	59.4	16.6	3.6

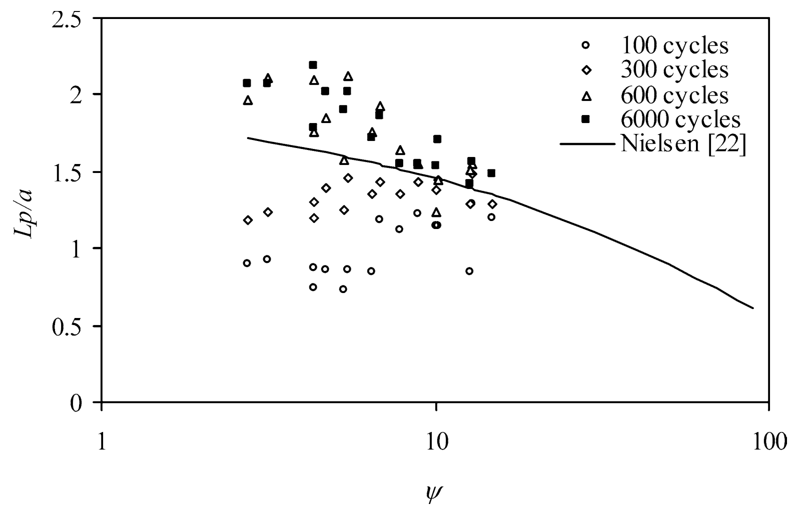

Fig. 11. Ripple length plotted as a function of mobility number ψ for different excitation cycles numbers and superimposed with Nielsen curve [22].

drift with a rather good agreement. A positive drift tends to increase ripple length while a negative one tends to decrease it. The ripple heights are given indicatively in Table 2 but no representation of these data is given due to the large uncertainty on the estimation of these low heights varying in the range from 2 to 6 pixels.

4.3. Correlation between ripple geometry dynamics and dimensionless parameters

For fully developed ripples, the non-dimensional wavelength is mainly a function of the mobility number. Therefore, this parameter has been chosen at once to examine further ripple formation. The ripple length L_p/a is shown in Fig. 11 as a function of the mobility number for different excitation cycles numbers distributed over the complete test. As can be seen, a saturation of the length is rapidly reached for the higher mobility numbers tested. Furthermore, in spite of some dispersion in the data, a change in trend of L_p/a curve can be observed. The length tends to increase with the mobility number for the lower numbers of excitation cycles. On the contrary, for the longer excitation times (6000 cycles), the length decreases when ψ number increases. This noted change in trend is due to both the slow growth of ripples when the mobility number takes low values and to the large values of the equilibrium length reached in these latter conditions. It is also worth pointing out that, as was suggested above, the noticeable scatter of data may be explained by the significant influence of the Reynolds number on the ripple length during the ripple formation stage.

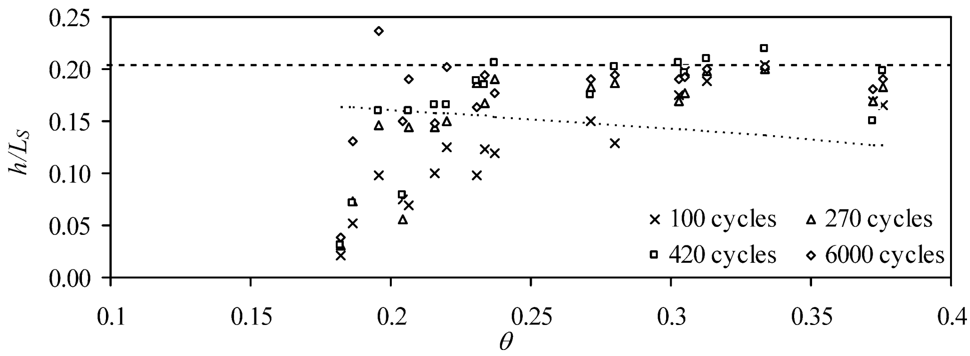

Fig. 12. Ripple steepness plotted versus Shields parameter θ for different excitation cycles numbers. Dotted line shows maximum equilibrium steepness [22].

The ripple steepness h/L_s is plotted on Fig. 12 against the Shields parameter θ for different numbers of excitation cycles (100, 270, 420 and 6000 cycles). Except for the two lower Shields values, the equilibrium steepness has been surely reached before 6000 excitation cycles. Furthermore, the dependence on Shields parameter is clearly demonstrated in the dynamical stage. On the other hand, at the equilibrium, the steepness remains constant in the Shields number range tested. It is consistent with Faraci et al. [3] results. According to Nielsen [22], for Shields parameters lower than 0.2, the slope of the equilibrium vortex ripples maintains at a maximum value with an angle close to the angle of repose of the sediment. The maximum steepness is then given by $0.32 \tan \phi_S$. Present experimental results suggest that the constancy of the steepness may extend to Shields values exceeding 0.3. The angle of ripple is equal to 30° which is lower than the measured angle of repose for the dry sediment (32.5°). During the development of the ripple, the ripple steepness appears to exceed slightly its equilibrium value due to a possible final superficial liquefaction of the sediment layer.

5. Conclusion

An experimental investigation of ripple dynamics under waves has been carried out in a channel, in conditions of moderate mobility numbers $(2 < \psi < 13)$. In the dynamical stage, many defects and irregularities are observed in ripple patterns. It has motivated the choice to study the transient ripple stage with a statistical approach. Distribution of wavelengths on large bidimensional top views of the ripple fields have been plotted. The technique used is the complex demodulation based on the application of Hilbert transform. The different stages of ripple formation are characterized by histogram of lengths distribution with typical shapes. The most probable wavelength L_p and the mean wavelength $\bar{L}$ are estimated and compared. It is shown that their respective evolution with time differ significantly but finally, for long times, a convergence is found. The mean length evolves rather regularly while the most probable one exhibits a progression by steps due to a low sensitivity to local changes in the extended pattern. Furthermore, it is demonstrated that, in conditions of low mobility numbers, a more present wavelength can remain constant for a short while in an evolving pattern characterized by a mean length which varies. This observed stage is a particular state during the rolling-grain ripples stage. The developed technique provides an accurate tool to measure wavelengths of temporary stable rolling-grain ripples. In these conditions, rolling-grain ripples are completely described by a constant value of L_p wavelength, a constant or weakly increasing ripple height and a steepness nearly equal to 0.1. The domain of parameters where the existence of “stable rolling-grain ripples” is surely observed is very restricted. In the moderate range of Reynolds number tested, the rolling-grain ripple length depends linearly on the boundary layer Reynolds number. The temporal evolution of ripple length can be represented in a dimensionless form using a typical time built on the mobility number. The general trend follows an exponential law as previously found but some features are not captured. In the dynamical stage, it is demonstrated that ripple length depends on both the mobility number and the Reynolds number.

The ripple steepness depends on the Shields parameter in the dynamical stage when it does not depend on this parameter at the equilibrium stage for the Shields range tested.

Finally, present work points out the important role played by defects in the patterns during the dynamical stage leading to the formation of equilibrium vortex ripple patterns. Further works should be directed towards the study of their influence.

References

[1] R.A. Bagnold, Motion of waves in shallow water: Interaction of waves and sand bottoms, Proc. Roy. Soc. London Ser. A 187 (1946) 1–15.

[2] J.F.A. Sleath, Sea Bed Mechanics, Wiley, 1994.
[3] C. Faraci, E. Foti, Geometry, migration and evolution of small-scale bedforms generated by regular and irregular waves, Coast. Engrg. 47 (2002) 35–52.
[4] S.I. Voropayev, G.B. McEachern, D.L. Boyer, H.J.S. Fernando, Dynamics of sand ripples and burial/scouring of cobbles in oscillatory flow, Appl. Ocean Res. 21 (1999) 249–261.
[5] M.A. Scherer, F. Melo, M. Marder, Sand ripples in an oscillating annular sand-water cell, Phys. Fluids A 11 (1) (1999).
[6] A. Stegner, J.E. Wesfreid, Dynamical evolution of sand ripples under water, Phys. Rev. E 60 (4) (1999).
[7] J.F.A. Sleath, On rolling-grain ripples, J. Hydraul. Res. 14 (1976) 69–81.
[8] A. Kaneko, H. Honji, Double structures of steady streaming in the oscillatory viscous flow over a wavy wall, J. Fluid Mech. 93 (1979) 727–736.
[9] P. Blondeaux, Sand ripples under sea waves, Part 1. Ripple formation, J. Fluid Mech. 218 (1990) 1–17.
[10] G. Vittori, P. Blondeaux, Sand ripples under sea waves, Part 2. Finite amplitude development, J. Fluid Mech. 218 (1990) 19–39.
[11] P. Blondeaux, E. Foti, G. Vittori, Migrating sea ripples, Eur. J. Mech. B Fluids 19 (2000) 285–301.
[12] K.H. Andersen, A particle model of rolling grain ripples under waves, Phys. Fluids 13 (1) (2001) 58–63.
[13] M. Manohar, Mechanics of bottom sediment movement due to wave action, U.S. Army Beach Erosion board, Tech. Memo 75, 1955.
[14] P. Blondeaux, J.F.A. Sleath, G. Vittori, Experimental data on sand ripples in an oscillatory flow, Rep. 01/88 Inst. Hydraulics University of Genoa, 1988.
[15] G. Rousseaux, A. Stegner, J.E. Wesfreid, Wavelength selection of rolling grain ripples in laboratory, Phys. Rev. E, Preprint.
[16] D.M. Hanes, V. Alymov, Y.S. Chang, C. Jette, Wave-formed sand ripples at Duck, North Carolina, J. Geophys. Res. 106 (10) (2001) 22575–22592.
[17] J. Brossard, A. Hémon, E. Rivoalen, Improved analysis of regular gravity waves and coefficient of reflexion using one or two moving probes, Coast. Engrg. 39 (2000) 193–212.
[18] I.G. Jonsson, Wave boundary layers and friction factors, in: Coast. Eng. Proc. 10th Conf. Tokyo 1, ASCE, 1966, pp. 127–146.
[19] K.E.B. Lofquist, Sand ripple growth in an oscillatory flow water tunnel, Tech. Paper 78 (5), U.S. Army Corps. Eng., Coast. Engrg. Res. Centre, 101 pp.
[20] P. Traykovski, A.E. Hay, J.D. Irish, J.F. Lynch, Geometry, migration, and evolution of wave orbital ripples at LEO-15, J. Geophys. Res. 104 (C1) (1999) 1505–1524.
[21] T. O'Donoghue, G.S. Clubb, Sand ripples generated by regular oscillatory flow, Coast. Engrg. 44 (2001) 101–115.
[22] P. Nielsen, Dynamics and geometry of wave-generated ripples, J. Geophys. Res. 86 (C7) (1981) 6467–6472.